
VARIATIONAL TRAJECTORY OPTIMIZATION OF ANISOTROPIC DIFFUSION SCHEDULES

Pengxi Liu*

Department of Electrical and Computer Engineering
Duke University
pengxi.liu@duke.edu

Zeyu Michael Li*

Department of Electrical and Computer Engineering
Duke University
zeyu.li030@duke.edu

Xiang Cheng

Department of Electrical and Computer Engineering
Duke University
xiang.cheng@duke.edu

ABSTRACT

We introduce a variational framework for diffusion models with anisotropic noise schedules parameterized by a matrix-valued path $M_t(\theta)$ that allocates noise across subspaces. Central to our framework is a trajectory-level objective that jointly trains the score network and *learns* $M_t(\theta)$, which encompasses general parameterization classes of matrix-valued noise schedules. We further derive an estimator for $\partial_\theta \nabla \log p_t$ that enables efficient optimization of the $M_t(\theta)$ schedule. For inference, we develop an efficiently-implementable reverse-ODE solver that is an anisotropic generalization of the second-order Heun discretization algorithm. Across CIFAR-10, AFHQv2, FFHQ, and ImageNet-64, our method consistently improves upon the baseline EDM model in all NFE regimes. Code is available at <https://github.com/lizeyu090312/anisotropic-diffusion-paper>.

Keywords Diffusion Model · Anisotropic Diffusion

1 Introduction

Diffusion models generate samples by *reversing* a gradual Gaussian noising process. Starting from data $x_0 \sim p_0$, a forward process produces a family of noisy variables $(x_t)_{t \geq 0}$ with density p_t that smoothly interpolates between the data distribution and a tractable Gaussian. A neural *score* model (parameters ϕ) is trained to approximate the score $\nabla_x \log p_t(x)$; given this score, sampling integrates a reverse-time SDE/ODE that transports p_T back to p_0 [1, 2, 3]. Nearly all modern diffusion pipelines assume *isotropic* forward noise, meaning that at time t , the covariance of total injected Gaussian noise is a scalar multiple of identity.

Matrix-valued (anisotropic) schedules. In this paper, we replace the scalar noise level by a *matrix-valued* covariance trajectory M_t and study how to *learn* it. Concretely, in the standard variance-exploding (VE) / Brownian formulation, the isotropic process adds noise with covariance tI ,

$$x_0 \sim p_0, \quad dx_t = dB_t \Leftrightarrow \quad dx_t = -\frac{1}{2} \nabla \log p_t(x_t) dt, \quad (1)$$

where B_t is standard Brownian motion and $*$ denotes convolution. We generalize this to anisotropic diffusion by instead considering a forward diffusion driven by a *matrix-valued diffusion coefficient*:

$$x_0 \sim p_0, \quad dx_t = (\partial_t M_t)^{1/2} dB_t \Leftrightarrow \quad dx_t = -\frac{1}{2} \partial_t M_t \nabla \log p_t(x_t) dt, \quad (2)$$

where $M_t(\theta)$ is a matrix-valued noise-schedule, with arbitrary parameterization θ , satisfying

$$M_0 = 0, \quad \partial_t M_t \succ 0 \quad \text{for all } t. \quad (3)$$

*Equal contribution.

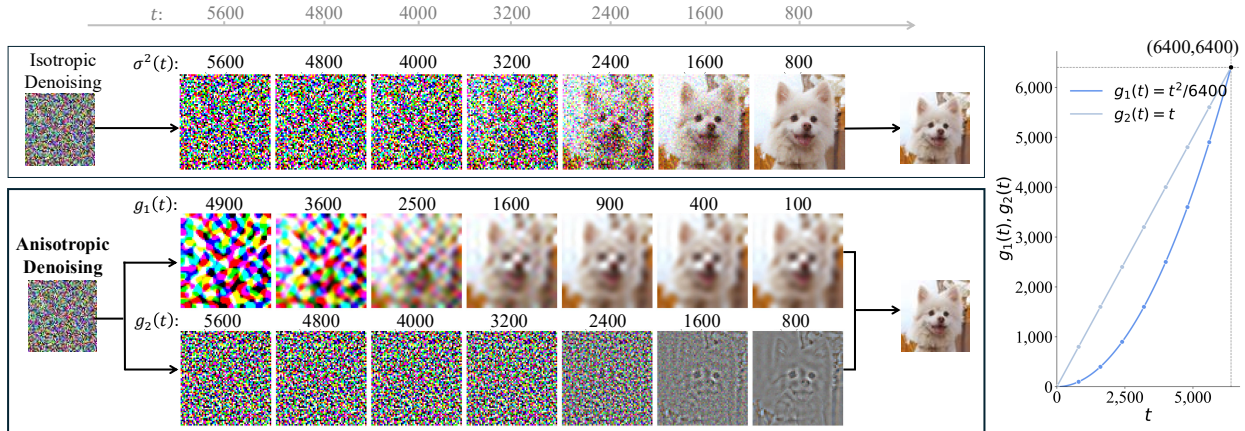


Figure 1: **Illustration of isotropic vs. anisotropic denoising.** Top: a standard isotropic sampler denoises all directions uniformly. Bottom: an anisotropic sampler with two DCT subspaces, V_1 (low frequency) and V_2 (high frequency) (Section 6). Columns show intermediate reconstructions as t decreases. The plot (right) displays learned subspace schedules $g_1(t)$ and $g_2(t)$; the former is denoised more aggressively, so low-frequency structure from V_1 emerges earlier, while high-frequency details from V_2 emerge later. **Illustration only:** in practice anisotropic and isotropic reconstruct different images, and the gap between g_1 and g_2 is typically smaller (see Fig. 2–5).

The power of anisotropy. Replacing a scalar schedule by a matrix path allows noise (and thus denoising effort) to be allocated differently across directions and time, better matching data geometry. Natural images concentrate energy in low spatial frequencies [4]; latent diffusion effectively separates coarse structure from fine detail [5]; video models benefit from temporally structured priors or decomposed noise [6, 7]; and multi-resolution generation often proceeds coarse-to-fine [8]. Figure 1 illustrates one such effect: low-frequency content can be denoised earlier than high-frequency details when the schedule is allowed to differ across subspaces.

A variational formulation of matrix trajectory is necessary. The flexibility of M_t comes with a price: the design space is enormous—instead of choosing a single scalar function, we must choose a trajectory in the cone of PSD matrices. In the isotropic VE case, the family of marginals is essentially one-dimensional: $p_t = p_0 * \mathcal{N}(0, \sigma(t)^2 I)$ depends on t only through the scalar variance $\sigma(t)^2$, so changing the schedule mainly *reparameterizes time* along the same curve of distributions. In contrast, different anisotropic paths $M_t(\theta)$ generally produce genuinely different marginals $p_t(\cdot; \theta)$ (even up to time reparameterization), and hence different score targets and reverse-time dynamics. This makes hand-crafted anisotropy brittle and motivates a principled, data-driven approach.

1.1 Main contributions

We develop a variational framework for *learning* anisotropic diffusion trajectories $M_t(\theta)$ jointly with a score model (parameters ϕ), rather than prescribing M_t by hand. We summarize our technical and empirical contributions below

(1) A general variational framework for learning anisotropic diffusion models.

1. We introduce a variational framework for anisotropic diffusion with *matrix-valued* noise path $M_t(\theta)$. Our framework is fully general and supports broad classes of $M_t(\theta)$, including interpretable frequency-band schedules and data-adaptive (class-conditional) PCA schedules (Section 6).
2. We propose a trajectory-level score-matching objective $L(\theta, \phi)$ (Section 3) that jointly trains the score network and learns $M_t(\theta)$ by minimizing mismatch between ideal and learned denoising dynamics along the reverse trajectory (with a pathwise change-of-measure interpretation).
3. We derive anisotropic reverse-ODE solvers by generalizing Euler and second-order Heun updates to matrix trajectories (Section 5), yielding closed-form steps expressed through increments of $M_t^{1/2}$ and implementable efficiently via structured matrix operations.

(2) An efficient schedule-gradient estimator for matrix-valued trajectories. Optimizing $M_t(\theta)$ is challenging because changing θ changes the entire forward family $p_t(\cdot; \theta)$, and thus requires $\partial_\theta \nabla \log p_t(x; \theta)$, which is not available from a network trained at a single θ . We derive a plug-in estimator of $\partial_\theta \nabla \log p_t(x; \theta)$ using only higher-

order x -directional derivatives of the network, implementable in **three backward passes** and independent of $\dim(\theta)$ (Theorem 4.1). We further introduce a *flow parameterization* that stabilizes scale across noise levels and reduces estimator variance (Section 4.2).

(3) Empirical validation of anisotropic trajectory learning. Across CIFAR-10, AFHQv2, FFHQ, and ImageNet-64 (Section 7), learned anisotropic trajectories are competitive with (and often improve upon) the EDM baseline under the standard evaluation protocol. The gains persist across solver budgets and schedule families, supporting the view that *learning the matrix trajectory improves score-matching and the resulting generative model*.

1.2 Related Work

Structured noising and anisotropy. Prior work introduces non-isotropic structure via edge-aware perturbations [9], correlated/blue-noise masks [10], subspace/frequency restrictions [11], and temporally structured priors for video [7, 6, 12]. In contrast, we learn a *global*, monotone PSD *matrix* trajectory $M_t(\theta)$ (e.g., DCT/PCA-parameterized) and optimize it *jointly* with the score network via a trajectory loss, allocating noise (and denoising effort) across *directions/subspaces*.

ELBO views and schedule learning. VDM [13] and the ELBO reinterpretation of common diffusion losses [14] relate *scalar* schedule learning to reweighting *noise levels*. MuLAN [15] learns (possibly input-conditional) *per-pixel* noise rates to tighten an ELBO for density estimation. Our formulation differs in that (i) $M_t(\theta)$ is *anisotropic* (reweights *directions*, not just levels), (ii) we derive a practical schedule-gradient estimator that accounts for the schedule-dependent score target, and (iii) we optimize the schedule to improve *sample quality*, yielding consistent FID gains.

2 Preliminaries

2.1 Anisotropic Diffusion: Process, Score, and Parameterizations

Recall the anisotropic diffusion process in (2). Let $M_t(\theta)$ denote the noise covariance at time t , parameterized by θ . p_t as defined in (2) has score given by

$$\nabla \log p_t(x; \theta) = M_t^{-1}(\theta) \mathbb{E}_{x_0|x_t=x} [x_0 - x_t], \quad (4)$$

where (x_0, x_t) are defined by the joint distribution $x_0 \sim p_0$ and $x_t = x_0 + \mathcal{N}(0, M_t)$. We provide a short proof in Lemma A.1 in Appendix A. In case of time-uniform isotropic diffusion (i.e. standard Brownian Motion), $M_t(\theta) = tI$, and the formula in (4) reduces to the standard score expression.

We parameterize a neural network $\text{net}(x, t, \phi)$ to approximate the score, we also define flow, a transformation of net whose norm is approximately time-invariant:

$$\text{net}(x, t, \phi) \approx \nabla \log p_t(x; \theta) \quad (5)$$

$$\text{flow}(x, t, \phi) := M_t^{1/2} \text{net}(x, t, \phi) \quad (6)$$

Continuous and discrete reverse ODE for anisotropic denoising. Recall the *forward ODE dynamics* as defined in (2): $dx_t = -\frac{1}{2} \partial_t M_t \nabla \log p_t(x_t) dt$. Given net in (5), the learned denoising ODE is given by the time-reversal of

$$d\bar{x}_t = -\frac{1}{2} \partial_t M_t(\theta) \text{net}(\bar{x}_t, t, \phi) dt, \quad (7)$$

Variance-preserving anisotropic diffusion. It is often more useful to consider the *variance preserving* anisotropic diffusion, which is simply a time-dependent linear-transformation of (2). Define

$$x_t^{VP} := (I + M_t(\theta))^{-1/2} x_t. \quad (8)$$

The choice of I above is based on the assumption that $\text{Cov}(x_0) \approx I$, which implies that $\text{Cov}(x_t^{VP}) \approx I$ for all t . Combining (8) with (2) gives the following dynamic:

$$\begin{aligned} dx_t^{VP} &= v(x_t, t; \theta) dt, \quad \text{where} \\ v(x, t; \theta) &:= -\frac{1}{2} (I + M_t(\theta))^{-1/2} \partial_t M_t(\theta) \nabla \log p_t(x; \theta) - \frac{1}{2} (I + M_t(\theta))^{-3/2} \partial_t M_t(\theta) x, \end{aligned} \quad (9)$$

where $v(x, t; \theta)$ is the *ideal* velocity field. Analogously, we define the *learned* velocity field

$$\begin{aligned} d\bar{x}_t^{VP} &= \bar{v}(x_t, t; \theta)dt, \quad \text{where} \\ \bar{v}(x, t; \theta, \phi) &:= -\frac{1}{2}(I + M_t(\theta))^{-1/2}\partial_t M_t(\theta)\text{net}(x, t, \phi) - \frac{1}{2}(I + M_t(\theta))^{-3/2}\partial_t M_t(\theta)x, \end{aligned} \quad (10)$$

3 Trajectory-Level Score Matching Loss

This section introduces our central training objective (11), which enables us to **jointly** learn a **matrix-valued** noise path $\{M_t(\theta)\}_{t \in [0, T]}$ together with a **score network** $\text{net}(x, t, \phi)$. At a high level, the loss measures a **trajectory-weighted score error** induced by the schedule $M_t(\theta)$, and it is designed so that (for any fixed θ) the optimal network recovers the true score (Lemma 3.1).

3.1 Defining the Trajectory Loss

Loss definition. We define our trajectory-level training objective as

$$\begin{aligned} L(\theta, \phi) &:= \mathbb{E}_{t \sim \text{Unif}[0, T], x_0 \sim p_0, \epsilon \sim \mathcal{N}(0, I)} \left[\left\| W_t(\theta) \left(M_t(\theta)^{1/2} \text{net}(x_0 + M_t(\theta)^{1/2} \epsilon, t, \phi) + \epsilon \right) \right\|_2^2 \right] \\ \text{where } W_t(\theta) &:= (I + M_t(\theta))^{-1/2} (\partial_t M_t(\theta)) M_t(\theta)^{1/2}. \end{aligned} \quad (11)$$

In words: we draw a noise level t , perturb data by $x_t := x_0 + M_t(\theta)^{1/2} \epsilon$, evaluate the score network at (x_t, t) , and penalize its deviation from the *noise target* $-\epsilon$, under a *matrix-valued* weight $W_t(\theta)$ determined by the trajectory $M_t(\theta)$. Since $x_t = x_0 + M_t(\theta)^{1/2} \epsilon$, we have $M_t(\theta)^{-1/2} \epsilon = -M_t(\theta)^{-1}(x_0 - x_t)$, so the network term inside (11) is trained to match the conditional denoising direction. The operator $W_t(\theta)$ serves as a *matrix-valued* weighting schedule that can emphasize different subspaces at different times, and it is exactly this dependence on $M_t(\theta)$ that allows us to *optimize the trajectory* θ .

Equivalence of loss to velocity mismatch norm. Recall from Section 2 that under the variance-preserving (VP) reparameterization (8), the *ideal* and *learned* VP velocity fields are $v(\cdot, t; \theta)$ and $\bar{v}(\cdot, t; \theta, \phi)$ as defined in (9) and (10). A natural trajectory-level principle is to choose (θ, ϕ) so that the learned denoising dynamics match the ideal ones along the reverse trajectory. The continuous-time form of this principle is the path integral

$$\int_0^T \mathbb{E}_{x_0 \sim p_0, \epsilon \sim \mathcal{N}(0, I)} \left[\|\bar{v}(x_t, t; \theta, \phi) - \tilde{v}(x_t, x_0, t; \theta)\|_2^2 \right] dt, \quad x_t = x_0 + M_t(\theta)^{1/2} \epsilon, \quad (12)$$

where $\tilde{v}(\cdot, x_0, t; \theta)$ is obtained from the ideal velocity $v(\cdot, t; \theta)$ by replacing the intractable score $\nabla \log p_t(\cdot; \theta)$ with the single-sample proxy $M_t(\theta)^{-1}(x_0 - x_t)$ (see the score identity (4)):

$$\tilde{v}(x_t, x_0, t; \theta) := -\frac{1}{2}(I + M_t(\theta))^{-1/2} \partial_t M_t(\theta) M_t(\theta)^{-1}(x_0 - x_t) - \frac{1}{2}(I + M_t(\theta))^{-3/2} \partial_t M_t(\theta) x_t. \quad (13)$$

Expanding \bar{v} and \tilde{v} , the common contraction term $-\frac{1}{2}(I + M_t)^{-3/2} \partial_t M_t x_t$ cancels, and (12) reduces to the compact matrix-weighted score-matching form (11) (up to an overall constant factor and the standard Monte Carlo approximation of the time integral by sampling t).

3.2 Key Properties and Interpretation

Exact score at optimality. As standard in the literature [16, 2], we show that for any fixed schedule $M_t(\theta)$ satisfying (3), the optimal network for $L(\theta, \phi)$ recovers the true score in the infinite-data/infinite-capacity limit:

Lemma 3.1 (Exact score at optimality). *Fix any schedule $M_t(\theta)$ satisfying (3). In the limit of infinite data and model capacity, the minimizer $\phi^*(\theta) = \arg \min_{\phi} L(\theta, \phi)$ satisfies*

$$\text{net}(x, t, \phi^*(\theta)) = \nabla_x \log p_t(x; \theta). \quad (14)$$

We defer the proof of Lemma 3.1 to Appendix B.1.

Connection to path-wise change-of-measure (Girsanov). The objective (12) is a path-wise integral of a velocity mismatch, aligning with the classical change-of-measure control suggested by Girsanov’s theorem. Concretely, for two processes $dx_t = v(x_t, t) dt + dB_t$ and $d\bar{x}_t = \bar{v}(\bar{x}_t, t) dt + dB_t$, the path-space KL is bounded by a constant times $\int_0^T \mathbb{E} [\|\bar{v}(x_t, t) - v(x_t, t)\|_2^2] dt$ (under standard regularity, e.g. Novikov’s condition). Related bounds have been used to control reverse *SDE* discretization error [17]. Our loss can be viewed as a tractable surrogate in this spirit: it replaces the intractable score-dependent v with the proxy velocity \tilde{v} in (13).

Consistency check: isotropic trajectory loss reduces to weighted score matching. When $M_t(\theta) = g(t; \theta)I$ for a scalar function g , the weighting operator $W_t(\theta)$ becomes the scalar function $\frac{\partial_t g(t; \theta)}{\sqrt{1+g(t; \theta)}}$. In Lemma A.2 (Appendix A), we formally prove the equivalence to a standard weighted score-matching objective. Thus, in the isotropic case, choosing $g(t; \theta)$ is essentially choosing a weighting over noise levels. Our main focus, however, is that (11) enables **optimization over matrix-valued trajectories**.

4 Optimization of the Trajectory Loss

This section explains how we *learn* the matrix-valued trajectory $M_t(\theta)$. We first emphasize the subtle but crucial relationship between θ and the learned network: the parametric model $\text{net}(x, t, \phi)$ has *no explicit* dependence on θ , but the *optimal* network for a given schedule *does* depend on θ , because it approximates the score of the schedule-dependent marginal $p_t(\cdot; \theta) = p_0 * \mathcal{N}(0, M_t(\theta))$. We therefore present schedule learning as the following bilevel problem:

Let $L(\theta, \phi)$ be as defined in (11). Define

$$\phi^*(\theta) \in \arg \min_{\phi} L(\theta, \phi), \quad \Leftrightarrow \quad H(\theta) := L(\theta, \phi^*(\theta)) = \min_{\phi} L(\theta, \phi). \quad (15)$$

From (15), the joint minimization over (θ, ϕ) is equivalent to

$$\min_{\theta, \phi} L(\theta, \phi) = \min_{\theta} H(\theta).$$

Lemma 3.1 implies that, in the infinite-data/capacity limit, $\text{net}(x, t, \phi^*(\theta)) = \nabla_x \log p_t(x; \theta)$ for any θ .

The challenge of computing $\partial_{\theta} H(\theta)$: When optimizing θ in (15), we need $\partial_{\theta} H(\theta)$. Because $H(\theta)$ evaluates the loss at the θ -dependent optimum $\phi^*(\theta)$, differentiating H involves computing the derivative of the optimum score field wrt θ , i.e. $\partial_{\theta} \text{net}(x, t, \phi^*(\theta)) \approx \partial_{\theta} \nabla \log p_t(x, \theta)$. Even though $\text{net}(x, t, \phi)$ does not depend on θ , an implicit dependency on θ is introduced via $\phi^*(\theta)$.

The difficulty arises because at any point during training, **we only observe the current value of ϕ** . There is no simple way to directly compute $\partial_{\theta} \text{net}(x, t, \phi^*(\theta))$ or even $\partial_{\theta} \phi^*(\theta)$. However, there is remarkable structure in $p_t(x, \theta) = p_0 * \mathcal{N}(0, M_t(\theta))$. By exploiting this fact, we show that $\partial_{\theta} \nabla \log p_t(x, \theta)$ can be written using **only derivatives wrt x , without explicit derivatives wrt θ** . In turn, this enables us to approximate $\partial_{\theta} \text{net}(x, t, \phi^*(\theta))$ using only x -derivatives of the network.

4.1 A Plug-in Approximation for $\partial_{\theta} \nabla \log p_t$ via Stochastic Calculus

Below we provide an identity for expressing the θ -derivative of the true score $\partial_{\theta} \nabla \log p_t(x, \theta)$ using terms that only depend on entries of $\nabla^2 \log p_t(x, \theta)$.

Theorem 4.1. *Let $\theta \in \mathbb{R}^c$ and let $j \in \{1, \dots, c\}$ be any coordinate. Then for all $x \in \mathbb{R}^d$,*

$$\begin{aligned} \partial_{\theta_j} \nabla \log p_t(x; \theta) &= \frac{1}{2} \sum_{i=1}^d \partial_r \partial_s \nabla \log p_t \left(x + r e_i + s \partial_{\theta_j} M_t(\theta) e_i; \theta \right) \Big|_{r=s=0} \\ &\quad + \partial_s \nabla \log p_t \left(x + s \partial_{\theta_j} M_t(\theta) \nabla \log p_t(x; \theta); \theta \right) \Big|_{s=0}. \end{aligned} \quad (16)$$

Let $\phi^*(\theta)$ be defined as in (15). Under sufficient model capacity and data,

$$\begin{aligned} \partial_{\theta_j} \text{net}(x, t, \phi^*(\theta)) &= \frac{1}{2} \sum_{i=1}^d \partial_r \partial_s \text{net} \left(x + r e_i + s \partial_{\theta_j} M_t(\theta) e_i, t, \phi^*(\theta) \right) \Big|_{r=s=0} \\ &\quad + \partial_s \text{net} \left(x + s \partial_{\theta_j} M_t(\theta) \text{net}(x, t, \phi^*(\theta)), t, \phi^*(\theta) \right) \Big|_{s=0}. \end{aligned} \quad (17)$$

We defer the proof to Appendix B.2.

4.2 Flow Parameterization and Variance Reduction

A practical concern is that $\|\text{net}(x, t, \phi)\|_2$ typically scales like $\|M_t(\theta)^{-1/2}\|_2$, which can vary significantly across noise levels and inflate gradient variance. We therefore work with the normalized vector field

$$\text{flow}(x, t, \phi) := M_t(\theta)^{1/2} \text{net}(x, t, \phi), \quad (18)$$

whose scale is approximately time-invariant. Using Theorem 4.1, we can also express $\partial_\theta \text{flow}$ in terms of x -directional derivatives:

Corollary 4.2. *Under the same setup as Theorem 4.1,*

$$\begin{aligned} \partial_\theta \text{flow}(x, t, \phi^*(\theta)) &= \frac{1}{2} \sum_{i=1}^d \partial_r \partial_s \text{flow}\left(x + r e_i + s \partial_\theta M_t(\theta) e_i, t, \phi^*(\theta)\right) \Big|_{r=s=0} \\ &\quad + \partial_s \text{flow}\left(x + s M_t(\theta)^{-1/2} \partial_\theta M_t(\theta) \text{flow}(x, t, \phi^*(\theta)), t, \phi^*(\theta)\right) \Big|_{s=0} \\ &\quad + \frac{1}{2} M_t(\theta)^{-1} (\partial_\theta M_t(\theta)) \text{flow}(x, t, \phi^*(\theta)). \end{aligned}$$

We defer the proof of Corollary 4.2 to Appendix B.3.

4.3 Final Optimization Formulation for $H(\theta) = \min_\phi L(\theta, \phi)$

We now clarify how the schedule gradient uses (17) (or equivalently Corollary 4.2). We emphasize that the additional $\partial_\theta \text{net}(x, t, \phi^*(\theta))$ term appears when differentiating the **outer value function** $H(\theta) = \min_\phi L(\theta, \phi)$, not when differentiating $L(\theta, \phi)$ with ϕ held fixed.

For notational clarity we treat θ as a scalar below; the vector case follows by applying the same derivation to each coordinate θ_j . Let $x_0 \sim p_0$, $\epsilon \sim \mathcal{N}(0, I)$, sample t as in Section 3, and set $x_t := x_0 + M_t(\theta)^{1/2} \epsilon$. Using the flow form of the loss, we verify that $L(\theta, \phi)$ of (11) is equivalent to

$$L(\theta, \phi) = \mathbb{E}_{x_0, \epsilon, t} \left[\left\| W_t(\theta) (\text{flow}(x_t, t, \phi) + \epsilon) \right\|_2^2 \right] \quad W_t(\theta) := (I + M_t(\theta))^{-1/2} \partial_t M_t(\theta) M_t(\theta)^{-1/2}. \quad (19)$$

We define the convenient notation $\ell(v, \epsilon, W) := \|W(\theta)(v + \epsilon)\|_2^2$, so that $L(\theta, \phi) = \mathbb{E}_{x_0, \epsilon, t} [\ell(\text{flow}(x_t, t, \phi), \epsilon, W_t(\theta))]$.

Chain rule for the outer objective. Define $\text{flow}_\theta^*(x, t) := \text{flow}(x, t, \phi^*(\theta))$ and recall $H(\theta) = L(\theta, \phi^*(\theta))$. Differentiating gives

$$\partial_\theta H(\theta) = \underbrace{\partial_\theta L(\theta, \phi) \Big|_{\phi=\phi^*(\theta)}}_{\text{explicit dependence through } M_t(\theta)} + \underbrace{\mathbb{E}_{x_0, \epsilon, t} \left[\left\langle \nabla_v \ell(\text{flow}(x_t, t, \phi^*(\theta)), \epsilon, W_t(\theta)), \partial_\theta \text{flow}(x_t, t, \phi^*(\theta)) \right\rangle \right]}_{\text{implicit dependence through the optimal score/flow field}}, \quad (20)$$

The second term on the RHS above uses the (per-sample) gradient of $\ell(v, \epsilon, t)$ with respect to v given by $\nabla_{\text{flow}} \ell_t = 2 \hat{W}_t(\theta)^\top \hat{W}_t(\theta) (v + \epsilon)$, this term isolates the dependence of $H(\theta)$ on $\phi^*(\theta)$. We estimate $\partial_\theta \text{flow}_\theta^*(x_t, t)$ using Corollary 4.2 (equivalently, estimate $\partial_\theta \text{net}_\theta^*$ using (17)). In practice, the expectation in (20) is approximated by minibatch averages over samples $(x_0^{(j)}, \epsilon^{(j)}, t^{(j)})$, for $j = 1 \dots \text{BatchSize}$.

5 Denoising Algorithms for Matrix Trajectories

This section describes sampling (denoising) given (i) a learned PSD matrix trajectory $M_t(\theta)$ and (ii) a trained network $\text{flow}(x, t, \phi)$, where

$$\text{flow}(x, t, \phi) \approx M_t(\theta)^{1/2} \nabla_x \log p_t(x; \theta).$$

We focus on reverse-time ODE sampling, which is the inference method used throughout our experiments. We remark that our method generalizes easily to the reverse-time SDE setting.

5.1 Reverse-time ODE in flow form and initialization

Using $\text{net}(x, t, \phi) = M_t(\theta)^{-1/2} \text{flow}(x, t, \phi)$, and the learned ODE from (7), the reverse-time ODE is equivalent to the time-reversal of the following:

$$d\bar{x}_t = -\frac{1}{2} \partial_t M_t(\theta) M_t(\theta)^{-1/2} \text{flow}(\bar{x}_t, t, \phi) dt, \quad (21)$$

For initialization we sample $\xi \sim \mathcal{N}(0, I)$ and set

$$\bar{x}_T := M_T(\theta)^{1/2} \xi, \quad (22)$$

with T chosen large enough that p_T is close to a centered Gaussian.

Why the solver uses increments of $M_t^{1/2}$. In this section, we will assume that the matrices $M_t(\theta)$ share eigenvectors and therefore commute with $\partial_t M_t(\theta)$. This assumption is not necessary, but helps significantly simplify the algebra. In Section 6, we discuss numerous examples of families of $M_t(\theta)$ which satisfy this assumption. Under this commutation,

$$\frac{1}{2} \partial_t M_t(\theta) M_t(\theta)^{-1/2} = \partial_t (M_t(\theta)^{1/2}),$$

so (21) becomes

$$d\bar{x}_t = -\partial_t (M_t(\theta)^{1/2}) \text{flow}(\bar{x}_t, t, \phi) dt. \quad (23)$$

This reveals that the natural step size for anisotropic denoising is the *matrix increment* $\Delta M_t^{1/2}$, directly generalizing the scalar EDM viewpoint where $M_t = \sigma(t)^2 I$ and $\Delta M_k^{1/2} = (\sigma_{k-1} - \sigma_k) I$.

5.2 Reverse Euler discretization

Let K be the number of solver steps and choose a discretization grid

$$0 = t_0 < t_1 < \dots < t_K = T. \quad (24)$$

Reverse-time integration proceeds from t_K down to t_0 . For convenience, define

$$U_k := M_{t_k}(\theta)^{1/2}, \quad \Delta U_k := U_k - U_{k-1} \quad (k = 1, \dots, K). \quad (25)$$

A first-order explicit Euler discretization of the *time-reversal* of (23) yields

$$\bar{x}_{t_{k-1}} = \bar{x}_{t_k} + \Delta U_k \text{flow}(\bar{x}_{t_k}, t_k, \phi), \quad k = 1, \dots, K. \quad (26)$$

We present the above Euler-Discretization scheme (26) mainly as a baseline derivation; in our experiments, second-order Heun consistently dominates Euler in FID per NFE.

5.3 Heun's second-order method for matrix trajectories

We now present the matrix-valued generalization of Heun's second-order algorithm. We inherit the notation from Section 5.2 above. Fix a secondary evaluation time $\hat{t}_k \in [t_{k-1}, t_k]$ and denote $\hat{U}_k := M_{\hat{t}_k}(\theta)^{1/2}$. Let

$$u_k := -\text{flow}(\bar{x}_{t_k}, t_k, \phi).$$

We form a predictor at \hat{t}_k by

$$\hat{x}_{\hat{t}_k} = \bar{x}_{t_k} + (\hat{U}_k - U_k) u_k, \quad \hat{u}_k := -\text{flow}(\hat{x}_{\hat{t}_k}, \hat{t}_k, \phi). \quad (27)$$

At any time $s \in [t_{k-1}, t_k]$, we approximate the intermediate flow field at s by the affine model

$$\tilde{u}(s) := u_k + (U(s) - U_k) (\hat{U}_k - U_k)^{-1} (\hat{u}_k - u_k), \quad U(s) := M_s(\theta)^{1/2}.$$

Substituting this approximation into (23) and integrating yields the closed-form second-order update

$$\bar{x}_{t_{k-1}} = \bar{x}_{t_k} + \Delta U_k u_k + \frac{1}{2} (\Delta U_k)^2 (\hat{U}_k - U_k)^{-1} (\hat{u}_k - u_k). \quad (28)$$

We defer the proof to Lemma A.3 in the appendix. When $\hat{t}_k = t_{k-1}$ (endpoint choice), we have $\hat{U}_k = U_{k-1}$ and (28) reduces to the familiar Heun form

$$\bar{x}_{t_{k-1}} = \bar{x}_{t_k} + \Delta U_k \frac{u_k + \hat{u}_k}{2},$$

which matches the standard scalar EDM/Heun update when $M_t = \sigma(t)^2 I$. In experiments we consider two choices of \hat{t}_k , i.e. $\hat{t}_k = t_{k-1}$ (endpoint) and $\hat{t}_k = (t_{k-1} + t_k)/2$ (midpoint).

The solver grid $\{t_k\}_{k=0}^K$ is treated as an orthogonal design choice. In our experiments, for given total step K , we take $t_1 \dots t_K$ to be a uniform grid over $[0 \dots T]$.

Efficient implementation under structured parameterizations. All updates require only (i) matrix-vector products with $M_t(\theta)^{1/2}$ and (ii) product of $(\hat{U}_k - U_k)^{-1}$ with vectors. Under the projector-based families in Section 6, these operations reduce to inexpensive subspace-wise scalings (and subspace-wise pseudoinverses), avoiding explicit $d \times d$ matrix square roots or dense linear algebra.

6 Practical Choices of Matrix Schedule $M_t(\theta)$

The framework in Sections 3–5 applies to arbitrary monotone PSD matrix trajectories $M_t(\theta)$. Below, we demonstrate a number of specific parametric families of $M_t(\theta)$. In each case, we verify that the parameterization satisfies: (i) **monotonicity** ($\partial_t M_t(\theta) \succeq 0$), (ii) **efficient evaluation** of matrix functions appearing in the loss and sampler (e.g. $M_t^{\pm 1/2}$ and $(I + M_t)^{-1/2}$), and (iii) **commutation of $\partial_t M_t(\theta)$ and $M_t(\theta)$** .

6.1 A subspace-schedule framework

We use a broad family based on an orthogonal decomposition of \mathbb{R}^d into subspaces. Let $\{P_j\}_{j=1}^J$ be *orthogonal projection matrices* such that $P_j = P_j^\top \succeq 0$, $P_j^2 = P_j$, $P_j P_k = 0$ for $j \neq k$, and $\sum_{j=1}^J P_j = I$. Let $\{g_j(\cdot; \theta)\}_{j=1}^J$ be nonnegative, nondecreasing scalar functions with $g_j(0; \theta) = 0$ and $g_j(T; \theta) = T$. In our experiments, each $g_j(\cdot; \theta)$ is parameterized by a monotone knot-based family (Appendix C), which ensures g_j is nondecreasing and differentiable in θ . We define the matrix-valued schedule

$$M_t(\theta) := \sum_{j=1}^J g_j(t; \theta) P_j, \quad (24)$$

so that $\partial_t M_t(\theta) = \sum_{j=1}^J \dot{g}_j(t; \theta) P_j \succeq 0$ whenever each g_j is nondecreasing. This construction therefore satisfies the monotonicity constraint (3) automatically. Because the P_j are mutually orthogonal projectors, any (scalar) matrix function f acts *subspace-wise*:

$$f(M_t(\theta)) = \sum_{j=1}^J f(g_j(t; \theta)) P_j. \quad (25)$$

In particular, the quantities needed by our loss and sampler— $M_t^{\pm 1/2}$, M_t^{-1} , and $(I + M_t)^{-1/2}$ —reduce to inexpensive scalings on each subspace. This also matches the solver structure in Section 5, where updates depend on increments of $M_t^{1/2}$; under (24), these increments are simply subspace-wise scalar increments.

The form of (24) separates:

- **Directions / subspaces** (the projectors $\{P_j\}$, determined by a basis choice and a grouping), and
- **Time allocation** (the scalar schedules $\{g_j(\cdot; \theta)\}$).

This separation lets us trade off interpretability and expressivity while keeping training and sampling efficient.

6.2 Schedule families used in experiments

We now list the concrete instances of (24) used in our experiments in Section 7.

(a) Isotropic schedule (warm-up / special case). Standard isotropic diffusion corresponds to $J = 1$ with $P_1 = I$, so $M_t(\theta) = g(t; \theta)I$. This serves as a sanity check and warm-up baseline; it also emphasizes that our framework strictly generalizes scalar schedule learning.

(b) Fixed structured basis (DCT subspaces). For images, we often choose a fixed orthonormal transform $U \in \mathbb{R}^{d \times d}$ exposing interpretable directions (e.g. a 2D-DCT basis; see Appendix F.2). Partition the basis indices into J groups defining subspaces S_1, \dots, S_J (ordered by decreasing frequency), and let P_j be the projector onto S_j . A particularly simple instance is $J = 2$: S_1 is a low-frequency subspace and $S_2 = S_1^\perp$ its complement, giving

$$M_t(\theta) = g_1^{\text{DCT}}(t; \theta) P_1 + g_2^{\text{DCT}}(t; \theta) P_2.$$

This parameterization yields an interpretable notion of anisotropy (coarse-to-fine denoising) while remaining cheap.

(c) Class-conditional PCA bases (data-dependent subspaces, shared schedules). To incorporate data geometry, we can make the *basis* depend on a class label $y \in \{1, \dots, C\}$ (in the case of ImageNet and CIFAR10). For each class y , compute a PCA basis from training samples in that class and form mutually orthogonal subspaces $\{S_j^{(y)}\}_{j=1}^J$ that partition \mathbb{R}^d (e.g. $S_1^{(y)}$ spans the top- k PCs and the remaining subspaces capture residual directions). Let $P_j^{(y)}$ be the projector onto $S_j^{(y)}$. We then define

$$M_t(\theta; y) = \sum_{j=1}^J g_j^{\text{PCA}}(t; \theta) P_j^{(y)}.$$

Here the *subspaces* vary with y while the scalar schedules are shared across classes, isolating the effect of a class-dependent geometry.

(d) Shared structured basis + class-conditional schedules. For class-conditional generation with a score network $\text{net}(x, t, y; \phi)$, we can instead keep the projectors fixed (e.g. DCT projectors $\{P_j\}$) and make the schedules class-specific:

$$M_t(\theta; y) = \sum_{j=1}^J g_{j,y}^{\text{DCT}}(t; \theta) P_j.$$

Even in the simple $J = 2$ case this yields $2C$ coupled scalar trajectories, making black-box search over θ impractical and motivating our gradient-based optimization of θ .

(e) Class-conditional PCA bases + class-conditional schedules (most expressive). Finally, we can let *both* the subspaces and schedules depend on class:

$$M_t(\theta; y) = \sum_{j=1}^J g_{j,y}^{\text{PCA}}(t; \theta) P_j^{(y)}.$$

This is the largest design space we consider. It can align anisotropic diffusion dynamics with class-dependent data geometry, but it also highlights why an efficient variational optimization scheme is needed.

Discussion: expressivity vs. efficiency. Across (a)–(e), the template (24) ensures that all matrix operations required by the trajectory loss and the anisotropic solvers reduce to subspace-wise scalings via (25). Increasing expressivity corresponds to increasing J , allowing class dependence, or making the basis data-dependent (PCA), while retaining tractable computation.

7 Experiments

We evaluate learned anisotropic diffusion schedules on four standard image generation benchmarks: CIFAR-10 (32×32) [18], AFHQv2 (64×64) [19], FFHQ (64×64) [20], and ImageNet-64 (64×64) [21]. All comparisons are against the EDM baseline [3], using the official EDM implementation and its recommended hyperparameter settings for each dataset/configuration.

Training protocol. Our models are initialized from the corresponding pretrained EDM networks and then fine-tuned while learning the schedule parameters θ (and continuing to update network parameters ϕ) as in (19). Across all datasets, fine-tuning consumes the equivalent of 1.2M image passes (as measured by total images processed). See Appendix D for full training details.

Evaluation protocol. We generate 50k samples and compute Fréchet Inception Distance (FID \downarrow). For both EDM and our method, we repeat sampling three times (independent random seeds) and report the *minimum* FID across the three runs, matching the EDM evaluation protocol [3]. We report results across a range of solver budgets measured by number of function evaluations (NFE), where one function evaluation corresponds to one forward pass of the score/flow network during sampling. For Heun’s second-order solver, each step uses two network evaluations, and when the secondary time is chosen as an endpoint ($\hat{t}_k = t_{k-1}$) the final evaluation at t_{k-1} is reused as the first evaluation of the next step. This yields the familiar odd NFE counts (approximately $2K - 1$ for K solver steps), consistent with EDM [3]. Unless otherwise noted, we use the Heun solver described in Section 5.

7.1 Schedule variants evaluated

We compare the following schedule families (see Section 6 for the corresponding parameterizations):

1. **EDM.** The original EDM baseline with isotropic schedule.
2. **Learned isotropic schedule g .** A single learned scalar schedule with $M_t = g(t; \theta)I$.
3. **Class-conditional isotropic schedules $\{g_y\}_{y=1}^C$.** One scalar schedule per class: $M_t(y) = g_y(t; \theta)I$.
4. **DCT anisotropic schedule $(g_1^{\text{DCT}}, g_2^{\text{DCT}})$.** A two-subspace matrix schedule with $J = 2$ in a fixed 2D-DCT basis (Appendix E), where the “low-frequency” subspace consists of the $(H/2) \times (H/2)$ lowest-frequency DCT modes (i.e., $H^2/4$ basis vectors) and the second subspace is its orthogonal complement: $M_t = g_1^{\text{DCT}}(t; \theta)P_1 + g_2^{\text{DCT}}(t; \theta)P_2$.

5. **PCA anisotropic schedule** $(g_1^{\text{PCA}}, g_2^{\text{PCA}})$. A two-subspace matrix schedule with $J = 2$ using class-conditional PCA bases (subspaces depend on class, schedules are shared), as described in Section 6.
6. **Class-conditional DCT anisotropic schedules** $\{(g_{1,y}^{\text{DCT}}, g_{2,y}^{\text{DCT}})\}_{y=1}^C$. Fixed DCT subspaces but class-specific scalar schedules.
7. **Class-conditional PCA anisotropic schedules** $\{(g_{1,y}^{\text{PCA}}, g_{2,y}^{\text{PCA}})\}_{y=1}^C$. The most expressive conditional variant we consider: both PCA subspaces and schedules depend on class.

Conditional vs. unconditional datasets. We consider CIFAR-10 and ImageNet-64 as class-conditional datasets. For CIFAR-10, which is relatively simple, we first train isotropic schedules, including both a global isotropic schedule and class-conditional isotropic schedules, as warm-up ablations. Building on this, we separately study the effects of class-conditional schedules and class-conditional bases. For ImageNet-64, due to its higher visual complexity, we directly adopt class-conditional isotropic schedules during warm-up. We then evaluate more expressive variants, including class-conditional schedules, class-conditional bases, and their combination. For AFHQv2 and FFHQ, which do not provide class labels, we primarily train structured-basis anisotropic schedules based on a fixed DCT decomposition with a global isotropic schedule g as an ablation for warm-up.

CIFAR-10									
Method	nfe 9	nfe 11	nfe 13	nfe 15	nfe 17	nfe 35	nfe 59	nfe 79	Best FID
EDM	35.52	14.37	6.694	4.231	3.027	1.829	1.868	1.890	1.829
g	4.241	3.087	2.650	2.431	2.328	1.815	1.820	1.835	1.815
$\{g_y\}_{y=1}^C$	3.691	3.090	2.735	2.582	2.480	1.831	1.829	1.841	1.829
$\{(g_{1,y}^{\text{DCT}}, g_{2,y}^{\text{DCT}})\}_{y=1}^C$	3.618	3.056	2.681	2.535	2.431	1.829	1.810	1.818	1.810
$(g_1^{\text{PCA}}, g_2^{\text{PCA}})$	3.839	2.900	2.538	2.332	2.213	1.851	1.803	1.803	1.803
AFHQv2									
Method	nfe 9	nfe 11	nfe 13	nfe 15	nfe 19	nfe 39	nfe 79	nfe 119	Best FID
EDM	27.98	13.66	7.587	4.746	2.986	2.075	2.042	2.046	2.042
g	4.657	3.085	2.584	2.463	2.332	2.091	2.041	2.042	2.041
$(g_1^{\text{DCT}}, g_2^{\text{DCT}})$	4.524	2.977	2.513	2.401	2.265	2.070	2.015	2.010	2.010
FFHQ									
Method	nfe 9	nfe 11	nfe 13	nfe 15	nfe 19	nfe 39	nfe 79	nfe 119	Best FID
EDM	57.14	29.39	15.81	9.769	5.169	2.575	2.391	2.374	2.374
g	68.35	27.92	13.44	8.097	3.958	2.265	2.242	2.281	2.242
$(g_1^{\text{DCT}}, g_2^{\text{DCT}})$	45.43	17.21	8.263	5.129	3.001	2.327	2.313	2.354	2.313
ImageNet-64									
Method	nfe 9	nfe 11	nfe 13	nfe 15	nfe 19	nfe 39	nfe 79	nfe 119	Best FID
EDM	35.32	15.19	8.160	5.458	3.586	2.428	2.294	2.276	2.276
$\{g_y\}_{y=1}^C$	8.416	5.907	4.749	4.079	3.366	2.455	2.314	2.296	2.296
$(g_1^{\text{PCA}}, g_2^{\text{PCA}})$	29.47	15.55	8.558	5.666	3.409	2.362	2.263	2.240	2.240
$\{(g_{1,y}^{\text{PCA}}, g_{2,y}^{\text{PCA}})\}_{y=1}^C$	8.366	5.823	4.626	3.992	3.282	2.378	2.259	2.239	2.239
$\{(g_{1,y}^{\text{DCT}}, g_{2,y}^{\text{DCT}})\}_{y=1}^C$	8.340	5.808	4.615	3.983	3.275	2.377	2.259	2.238	2.238

Table 1: FID \downarrow vs. NFE across datasets (50k samples). See section 7 for description of each method. For each method (both EDM and ours), we perform 3 independent random generations of 50k images and report the minimum FID across the three runs. *Bold* = per-NFE best. *Blue* = Best FID lower than EDM.

7.2 Discussion of results

Table 1 reports FID across solver budgets (NFE). Figures 2–5 (Appendix E) visualize the learned schedules and anisotropy ratios.

(i) **Consistent FID improvement over EDM baseline.** At the best-performing NFE in Table 1, we observe consistent improvements over EDM: CIFAR-10 improves from 1.829 (EDM) to 1.803 (PCA schedule); AFHQv2 improves

from 2.042 to 2.010 (DCT anisotropic); FFHQ improves from 2.374 to 2.242 (learned isotropic g); and ImageNet-64 improves from 2.276 to 2.238 (class-conditional DCT anisotropic). These gains persist across multiple NFE settings.

(iii) Matrix-valued anisotropy demonstrates benefits. Beyond the isotropic warm-up, matrix-valued schedules are often beneficial. On CIFAR-10 and AFHQv2, anisotropic variants improve upon EDM baseline or learned isotropic schedules across a wide range of NFES. On ImageNet-64, class-conditional anisotropic variants are the strongest, with $\{(g_{1,y}^{\text{DCT}}, g_{2,y}^{\text{DCT}})\}_{y=1}^C$ achieving the best FID (2.238).

(iv) Class-conditional variants matter most on complex conditional data. On both CIFAR-10 and ImageNet-64, class-conditional variants outperform their global counterparts. On CIFAR-10, class-conditional bases $(g_1^{\text{PCA}}, g_2^{\text{PCA}})$ achieve the best FID of 1.803. On ImageNet-64, class-conditional schedules $\{(g_{1,y}^{\text{DCT}}, g_{2,y}^{\text{DCT}})\}_{y=1}^C$ yield the best FID of 2.238. These results indicate that class-dependent schedule parameterizations are beneficial in practice.

8 Conclusion

We introduced a variational framework for learning *anisotropic* diffusion models by replacing the scalar noise schedule with a *monotone PSD, matrix-valued* trajectory $M_t(\theta)$ that allocates noise (and denoising effort) across directions and subspaces. Central to the framework is a *trajectory-level* score-matching objective that jointly trains the score network and optimizes the schedule, and admits a natural *pathwise change-of-measure* interpretation: the loss controls a tractable surrogate of the discrepancy between ideal and learned dynamics integrated along full trajectories. In the isotropic special case, the formulation reduces to standard weighted score matching—a useful consistency check—but its main purpose is to enable principled optimization over general matrix-valued schedules.

To make trajectory optimization practical, we derived an efficient plug-in estimator for schedule gradients using higher-order directional derivatives of the network, together with a flow parameterization that stabilizes scale across noise levels and reduces variance. For inference, we developed anisotropic reverse-time ODE solvers by generalizing Euler and second-order Heun updates to matrix trajectories, yielding closed-form steps expressed through increments of $M_t^{1/2}$ that can be implemented efficiently under structured parameterizations.

Empirically, we observe consistent improvements over the baseline across a wide range of datasets and settings; strongest performance was observed for complex class-conditional matrix schedules, underscoring the importance of an efficient variational approach to selecting anisotropic trajectories.

Looking forward, it is promising to expand the space of efficiently-computable matrix trajectories beyond orthogonal projector decompositions and to explore richer conditioning, as well as other modalities.

References

- [1] Jonathan Ho, Ajay Jain, and Pieter Abbeel. Denoising diffusion probabilistic models. *Advances in neural information processing systems*, 33:6840–6851, 2020.
- [2] Yang Song, Jascha Sohl-Dickstein, Diederik P. Kingma, Abhishek Kumar, Stefano Ermon, and Ben Poole. Score-based generative modeling through stochastic differential equations. In *International Conference on Learning Representations (ICLR)*, 2021.
- [3] Tero Karras, Miika Aittala, Timo Aila, and Samuli Laine. Elucidating the design space of diffusion-based generative models. *Advances in neural information processing systems*, 35:26565–26577, 2022.
- [4] Daniel Ruderman and William Bialek. Statistics of natural images: Scaling in the woods. *Advances in neural information processing systems*, 6, 1993.
- [5] Robin Rombach, Andreas Blattmann, Dominik Lorenz, Patrick Esser, and Björn Ommer. High-resolution image synthesis with latent diffusion models. In *Proceedings of the IEEE/CVF conference on computer vision and pattern recognition*, pages 10684–10695, 2022.
- [6] Songwei Ge, Seungjun Nah, Guilin Liu, Tyler Poon, Andrew Tao, Bryan Catanzaro, David Jacobs, Jia-Bin Huang, Ming-Yu Liu, and Yogesh Balaji. Preserve your own correlation: A noise prior for video diffusion models. In *Proceedings of the IEEE/CVF International Conference on Computer Vision*, pages 22930–22941, 2023.
- [7] Zhengxiong Luo, Dayou Chen, Yingya Zhang, Yan Huang, Liang Wang, Yujun Shen, Deli Zhao, Jingren Zhou, and Tieniu Tan. Videofusion: Decomposed diffusion models for high-quality video generation. *arXiv preprint arXiv:2303.08320*, 2023.

- [8] Keyu Tian, Yi Jiang, Zehuan Yuan, Bingyue Peng, and Liwei Wang. Visual autoregressive modeling: Scalable image generation via next-scale prediction. *Advances in neural information processing systems*, 37:84839–84865, 2024.
- [9] Jente Vandersanden, Sascha Holl, Xingchang Huang, and Gurprit Singh. Edge-preserving noise for diffusion models. 2024.
- [10] Xingchang Huang, Corentin Salaun, Cristina Vasconcelos, Christian Theobalt, Cengiz Oztireli, and Gurprit Singh. Blue noise for diffusion models. In *ACM SIGGRAPH 2024 conference papers*, pages 1–11, 2024.
- [11] Bowen Jing, Gabriele Corso, Renato Berlinghieri, and Tommi Jaakkola. Subspace diffusion generative models. In *European conference on computer vision*, pages 274–289. Springer, 2022.
- [12] Pascal Chang, Jingwei Tang, Markus Gross, and Vinicius C Azevedo. How i warped your noise: a temporally-correlated noise prior for diffusion models. *arXiv preprint arXiv:2504.03072*, 2025.
- [13] Diederik Kingma, Tim Salimans, Ben Poole, and Jonathan Ho. Variational diffusion models. *Advances in neural information processing systems*, 34:21696–21707, 2021.
- [14] Diederik Kingma and Ruiqi Gao. Understanding diffusion objectives as the elbo with simple data augmentation. *Advances in Neural Information Processing Systems*, 36:65484–65516, 2023.
- [15] Subham Sahoo, Aaron Gokaslan, Christopher M De Sa, and Volodymyr Kuleshov. Diffusion models with learned adaptive noise. *Advances in Neural Information Processing Systems*, 37:105730–105779, 2024.
- [16] Yang Song and Stefano Ermon. Generative modeling by estimating gradients of the data distribution. *Advances in neural information processing systems*, 32, 2019.
- [17] Sitan Chen, Sinho Chewi, Jerry Li, Yuanzhi Li, Adil Salim, and Anru R Zhang. Sampling is as easy as learning the score: theory for diffusion models with minimal data assumptions. *arXiv preprint arXiv:2209.11215*, 2022.
- [18] Alex Krizhevsky, Geoffrey Hinton, et al. Learning multiple layers of features from tiny images. 2009.
- [19] Yunjey Choi, Youngjung Uh, Jaejun Yoo, and Jung-Woo Ha. Stargan v2: Diverse image synthesis for multiple domains. In *Proceedings of the IEEE/CVF conference on computer vision and pattern recognition*, pages 8188–8197, 2020.
- [20] Tero Karras, Samuli Laine, and Timo Aila. A style-based generator architecture for generative adversarial networks. In *Proceedings of the IEEE/CVF conference on computer vision and pattern recognition*, pages 4401–4410, 2019.
- [21] Jia Deng, Wei Dong, Richard Socher, Li-Jia Li, Kai Li, and Li Fei-Fei. Imagenet: A large-scale hierarchical image database. In *2009 IEEE conference on computer vision and pattern recognition*, pages 248–255. Ieee, 2009.

A Additional Lemmas

Lemma A.1. *If x_t evolves as either one of the two processes:*

1. $(x_t - x_0) \sim \mathcal{N}(0, M_t(\theta))$
2. $dx_t = -\frac{1}{2}\partial_t M_t(\theta)\nabla \log p_t(x_t; \theta)dt$,

where $p_t(x; \theta) := p_0 * \mathcal{N}(0, M_t(\theta))$, then the score above is the conditional expectation

$$\nabla \log p_t(x; \theta) = M_t^{-1}(\theta)\mathbb{E}_{x_0|x_t=x}[x_0 - x_t],$$

where (x_0, x_t) are defined by the joint distribution $x_0 \sim p_0$ and $x_t = x_0 + \mathcal{N}(0, M_t)$.

Proof of Lemma A.1. Fix t and θ , and write $\Sigma := M_t(\theta)$. For notational simplicity we suppress the dependence on (t, θ) when clear. The marginal $p_t(\cdot; \theta)$ is the Gaussian convolution

$$p_t(x; \theta) = \int_{\mathbb{R}^d} p_0(x_0) \varphi_\Sigma(x - x_0) dx_0, \quad \varphi_\Sigma(z) := (2\pi)^{-d/2} |\Sigma|^{-1/2} \exp\left(-\frac{1}{2}z^\top \Sigma^{-1}z\right).$$

Assuming $\Sigma \succ 0$, we may differentiate under the integral sign to obtain

$$\nabla_x p_t(x; \theta) = \int p_0(x_0) \nabla_x \varphi_\Sigma(x - x_0) dx_0.$$

Since $\nabla_x \varphi_\Sigma(x - x_0) = \Sigma^{-1}(x_0 - x) \varphi_\Sigma(x - x_0)$, we get

$$\nabla_x p_t(x; \theta) = \Sigma^{-1} \int p_0(x_0) (x_0 - x) \varphi_\Sigma(x - x_0) dx_0.$$

Dividing by $p_t(x; \theta)$ yields

$$\nabla_x \log p_t(x; \theta) = \Sigma^{-1} \frac{\int p_0(x_0) (x_0 - x) \varphi_\Sigma(x - x_0) dx_0}{\int p_0(x_0) \varphi_\Sigma(x - x_0) dx_0} = \Sigma^{-1} \mathbb{E}[x_0 - x \mid x_t = x],$$

where the conditional distribution is $p(x_0 \mid x_t = x) \propto p_0(x_0) \varphi_\Sigma(x - x_0)$. Finally, since $x_t = x$ on the conditioning event, $x_0 - x = x_0 - x_t$, giving the stated identity. \square

Lemma A.2. *For any $w(t)$, there exists a $g_t(\theta)$ and constant c , such that for any $h(t)$*

$$\int_0^T \frac{(\partial_t g_t(\theta))^2}{1 + g_t(\theta)} h(g_t(\theta)) dt = c \int_0^T w(t) h(t) dt.$$

Proof of Lemma A.2. Let $w : [0, T] \rightarrow (0, \infty)$ be measurable and define

$$\Phi(x) := \int_0^x \frac{ds}{(1+s)w(s)} < \infty.$$

Then, to prove this Lemma, it is sufficient to show there exist a $c = \frac{\Phi(T)}{T} > 0$ and a strictly increasing continuous function $g : [0, T] \rightarrow [0, T]$ with $g(0) = 0$, $g(T) = T$ such that

$$\frac{g'(g^{-1}(t))}{1 + t} = cw(t) \text{ for all } t.$$

where $c = \Phi(T)/T$.

Define g implicitly by $\Phi(g(t)) = ct$ for $(0 \leq t \leq T)$, i.e. $g(t) = \Phi^{-1}(ct)$. Differentiating $\Phi(g(t)) = ct$ with respect to t yields the separable ODE $g'(t) = (1 + g(t))cw(g(t))$, and with $r = g(t)$ this is $\frac{g'(g^{-1}(r))}{1+r} = cw(r)$. Hence, we derive an expression for g involving a constant c and any w . Monotonicity of $g(t)$ follows since $w > 0$ and $c > 0$ imply $g'(t) > 0$.

Substituting into $c \int_0^T w(t) h(t) dt$, we get

$$c \int_0^T w(r) h(r) dr = \int_0^T \frac{g'(t)}{1 + g(t)} h(g(t)) g'(t) dt.$$

\square

Lemma A.3. Assume $M_{\bar{t}}$ commutes with $\partial_{\bar{t}}M_{\bar{t}}$. Let \tilde{u} be as defined in Section 5. Then

$$\begin{aligned} & \int_{t_k}^{t_{k-1}} (\partial_s M_s^{1/2}) \tilde{u}(s) ds \\ &= (M_{t_k}^{1/2} - M_{t_{k-1}}^{1/2}) (\text{flow}(\tilde{x}_{t_k}, t_k)) - \frac{1}{2} (M_{t_{k-1}}^{1/2} - M_{t_k}^{1/2})^2 (M_{\hat{t}_k}^{1/2} - M_{t_k}^{1/2})^{-1} \cdot (\text{flow}(\hat{x}_{\hat{t}_k}, \hat{t}_k) - \text{flow}(\tilde{x}_{t_k}, t_k)). \end{aligned}$$

Proof. Recall our notation that

$$u_k := \text{flow}(\bar{x}_{t_k}, t_k, \phi), \quad \hat{u}_k := -\text{flow}(\hat{x}_{\hat{t}_k}, \hat{t}_k, \phi).$$

$$\begin{aligned} & \int_{t_k}^{t_{k-1}} (\partial_s M_s^{1/2}(\theta)) \tilde{u}(s) ds \\ &= \int_{t_k}^{t_{k-1}} (\partial_s M_s^{1/2}(\theta)) \left(u_k + (M_s^{1/2}(\theta) - M_{t_k}^{1/2}(\theta)) (M_{\hat{t}_k}^{1/2}(\theta) - M_{t_k}^{1/2}(\theta))^{-1} (\hat{u}_k - u_k) \right) ds \\ &= \left(M_{t_{k-1}}^{1/2}(\theta) - M_{t_k}^{1/2}(\theta) \right) u_k + \int_{t_k}^{t_{k-1}} (\partial_s M_s^{1/2}(\theta)) (M_s^{1/2}(\theta) - M_{t_k}^{1/2}(\theta)) ds (M_{\hat{t}_k}^{1/2}(\theta) - M_{t_k}^{1/2}(\theta))^{-1} (\hat{u}_k - u_k) \\ &= \left(M_{t_{k-1}}^{1/2}(\theta) - M_{t_k}^{1/2}(\theta) \right) u_k + \frac{1}{2} (M_{t_{k-1}}^{1/2}(\theta) - M_{t_k}^{1/2}(\theta))^2 (M_{\hat{t}_k}^{1/2}(\theta) - M_{t_k}^{1/2}(\theta))^{-1} (\hat{u}_k - u_k). \end{aligned}$$

□

B Proofs

B.1 Proof of Lemma 3.1

We simplify the term inside the Euclidean norm in (12):

$$\begin{aligned} & \bar{v}(x_t, t; \theta, \phi) - \tilde{v}(x_t, x_0, t; \theta) \\ &= (I + M_t(\theta))^{-1/2} \partial_t M_t(\theta) (M_t^{-1}(\theta)(x_0 - x_t) - \text{net}(x_t, t, \phi)). \end{aligned}$$

Let M_{all} denote $(I + M_t(\theta))^{-1/2} \partial_t M_t(\theta)$. Let $V : \mathbb{R}^d \rightarrow \mathbb{R}^d$ be an arbitrary vector field.

We can minimize the expectation pointwise at each x_t . We can rewrite the expectation

$$\mathbb{E}_{x_0, \epsilon} \left[\left\| M_{\text{all}}(\text{net}(x_t, t, \phi) - M_t^{-1}(\theta)(x_0 - x_t)) \right\|_2^2 \right]$$

as

$$\begin{aligned} & \mathbb{E}_{x_0, \epsilon} \left[\left\| M_{\text{all}}(V(x_t) - M_t^{-1}(\theta)(x_0 - x_t)) \right\|_2^2 \right] \\ &= \mathbb{E}_{x_t} \left[\mathbb{E}_{x_0, \epsilon | x_t} \left[\left\| M_{\text{all}}(V(x_t) - M_t^{-1}(\theta)(x_0 - x_t)) \right\|_2^2 \right] \right] \end{aligned}$$

by the law of iterated expectation.

$$\begin{aligned} & \arg \min_{v \in \mathbb{R}^d} \mathbb{E}_{x_0, \epsilon | x_t} \left[(v - M_t^{-1}(\theta)(x_0 - x_t))^\top \right. \\ & \quad \left. M_{\text{all}}(v - M_t^{-1}(\theta)(x_0 - x_t)) \right] \\ &= M_t^{-1}(\theta) \mathbb{E}_{x_0, \epsilon | x_t} [x_0 - x_t] = \nabla \log p_t(x; \theta). \end{aligned}$$

The above equality follows from (4). The penultimate equality follows from the fact that $\arg \min_{a \in \mathbb{R}^d} (b-a)^\top Q(b-a) = b$ for any PSD matrix Q . Note that $\partial_t M_t = A_t^2$ is PSD, and M_t being the covariance in the diffusion process is also PSD. Hence, assuming that $\partial_t M_t$ commutes with M_t , M_{all} is PSD.

B.2 Proof of Theorem 4.1

To simplify notation, we will drop the index j and treat θ as a scalar. The general proof for $\theta \in \mathbb{R}^c$ follows by repeating the proof for each θ_j , while holding all other θ'_k s fixed. Recall that $p_t(\cdot; \theta) = p_0 * \mathcal{N}(0, M_t(\theta))$. By the the heat equation (applied to $\partial_\theta M_t(\theta)$ instead of $\partial_t M_t(\theta)$),

$$\begin{aligned} & \partial_\theta p_t(x; \theta) \\ &= \frac{1}{2} \mathbf{div}(p_t(x; \theta) \partial_\theta M_t(\theta) \nabla \log p_t(x; \theta)) \\ &= \frac{1}{2} p_t(x; \theta) \mathbf{div}(\partial_\theta M_t(\theta) \nabla \log p_t(x; \theta)) \\ & \quad + \frac{1}{2} p_t(x; \theta) \langle \nabla \log p_t(x; \theta), \partial_\theta M_t(\theta) \nabla \log p_t(x; \theta) \rangle. \end{aligned}$$

Dividing both sides by $p_t(x; \theta)$ gives

$$\begin{aligned} & \partial_\theta \log p_t(x; \theta) \\ &= \frac{1}{2} \mathbf{div}(\partial_\theta M_t(\theta) \nabla \log p_t(x; \theta)) \\ & \quad + \frac{1}{2} \langle \nabla \log p_t(x; \theta), \partial_\theta M_t(\theta) \nabla \log p_t(x; \theta) \rangle \\ &= \frac{1}{2} \sum_i \langle \partial_\theta M_t(\theta) e_i, \nabla^2 \log p_t(x; \theta) e_i \rangle \\ & \quad + \frac{1}{2} \langle \nabla \log p_t(x; \theta), \partial_\theta M_t(\theta) \nabla \log p_t(x; \theta) \rangle \\ &= \frac{1}{2} \sum_i \langle \partial_\theta M_t(\theta) e_i, \partial_c \nabla \log p_t(x + c e_i; \theta) \rangle \\ & \quad + \frac{1}{2} \langle \nabla \log p_t(x; \theta), \partial_\theta M_t(\theta) \nabla \log p_t(x; \theta) \rangle. \end{aligned}$$

Taking a derivative wrt x gives

$$\begin{aligned} & \partial_\theta \nabla \log p_t(x; \theta) \\ &= \frac{1}{2} \sum_i \langle \partial_\theta M_t(\theta) e_i, \partial_c \nabla^2 \log p_t(x + c e_i; \theta) \rangle \\ & \quad + \langle \partial_\theta M_t(\theta) \nabla \log p_t(x; \theta), \nabla^2 \log p_t(x; \theta) \rangle \\ &= \frac{1}{2} \sum_i \partial_r \partial_s \nabla \log p_t(x + r e_i + s \partial_\theta M_t(\theta) e_i; \theta) \\ & \quad + \partial_s \nabla \log p_t(x + s \partial_\theta M_t(\theta) \nabla \log p_t(x; \theta); \theta). \end{aligned}$$

This concludes the proof of (17). To prove (17), we combine (17) with the guarantee that $\text{net}(x, t, \phi^*(\theta)) = \nabla \log p_t(x; \theta)$ from Lemma 3.1.

B.3 Proof of Corollary 4.2

Recall that

$$\text{flow}(x; \theta) = M_t(\theta)^{1/2} \text{net}(x; \theta) = M_t(\theta)^{1/2} \nabla \log p_t(x; \theta).$$

Recall also from (17) that

$$\begin{aligned} & \partial_\theta \text{net}(x, t, \phi^*(\theta)) \\ &= \frac{1}{2} \sum_{i=1}^d \partial_r \partial_s \text{net}(x + r e_i + s \partial_\theta M_t(\theta) e_i, t, \phi^*(\theta)) \\ & \quad + \partial_s \text{net}(x + s \partial_\theta M_t(\theta) \text{net}(x, t, \phi^*(\theta)), t, \phi^*(\theta)). \end{aligned}$$

Combining the two equations above:

$$\begin{aligned}
& \partial_\theta \text{flow}(x; \phi^*(\theta)) \\
&= M_t(\theta)^{1/2} \partial_\theta \text{net}(x; \phi^*(\theta)) + \frac{1}{2} M_t(\theta)^{-1/2} (\partial_\theta M_t(\theta)) \text{net}(x; \phi^*(\theta)) \\
&= \frac{1}{2} \sum_i M_t(\theta)^{1/2} \partial_r \partial_s \text{net}(x + r e_i + s \partial_\theta M_t(\theta) e_i; \phi^*(\theta)) \\
&\quad + M_t(\theta)^{1/2} \partial_s \text{net}(x + s \partial_\theta M_t(\theta) \text{net}(x; \phi^*(\theta)); \phi^*(\theta)) + \frac{1}{2} M_t(\theta)^{-1/2} (\partial_\theta M_t(\theta)) \text{net}(x; \phi^*(\theta)) \\
&= \frac{1}{2} \sum_i \partial_r \partial_s \text{flow}(x + r e_i + s \partial_\theta M_t(\theta) e_i; \phi^*(\theta)) \\
&\quad + \partial_s \text{flow}(x + s M_t(\theta)^{-1/2} \partial_\theta M_t(\theta) \text{flow}(x; \phi^*(\theta)); \phi^*(\theta)) + \frac{1}{2} M_t(\theta)^{-1} (\partial_\theta M_t(\theta)) \text{flow}(x; \phi^*(\theta)).
\end{aligned}$$

C Implementation Details of g_i

For a fixed set of node locations $0 = \tau_0 < \tau_1 < \dots < \tau_{K-1} = T$, the subspace noise schedule is defined in log-space between the smallest and largest variance values $g(0) = g_0$ and $g(T) = T$. The trainable parameters $\theta = (\theta_1, \dots, \theta_{K-1})$ define a collection of strictly positive increments

$$s_i = \text{softplus}(\theta_i), \quad i = 1, \dots, K-1,$$

These increments are then rescaled by α so that their sum exactly matches the total log-gap between the endpoints,

$$\alpha = \frac{\log T - \log g_0}{\sum_{i=1}^{K-1} s_i}.$$

The log-values at the nodes are constructed by cumulative summation,

$$\ell_0 = \log g_0, \quad \ell_j = \ell_0 + \sum_{i=1}^j \alpha s_i, \quad j = 1, \dots, K-1,$$

so that $\ell_{K-1} = \log T$.

Given a time $t \in [0, T]$, one locates the enclosing interval $[\tau_{j-1}, \tau_j]$ and computes the normalized position

$$p(t) = \frac{t - \tau_{j-1}}{\tau_j - \tau_{j-1}}.$$

The value of $g(t)$ is then obtained by linearly interpolating between successive log-nodes and exponentiating:

$$\log g(t) = (1 - p(t)) \ell_{j-1} + p(t) \ell_j, \quad g(t) = \exp(\log g(t)).$$

Within each interval the derivative takes the simple form

$$g'(t) = g(t) \frac{\ell_j - \ell_{j-1}}{\tau_j - \tau_{j-1}}.$$

D Detailed Training Setup

Initialization. All experiments are initialized from the corresponding pretrained EDM checkpoints. We load both raw network weights and their exponential moving average (EMA) counterparts. When learning diffusion schedules, we initialize schedule parameters from a pretrained isotropic schedule model. For conditional variants, schedule parameters are instantiated per class. If class-wise isotropic schedules are available, they are used for initialization; otherwise, a shared global schedule is copied across classes.

Joint optimization of network and schedule. We jointly optimize network parameters ϕ and schedule parameters θ using Adam ($\beta_1 = 0.9$, $\beta_2 = 0.999$, $\epsilon = 10^{-8}$). Network and schedule parameters use separate learning rates. Gradients are accumulated over multiple micro-batches to achieve the target effective batch size. After backpropagation, gradients are explicitly sanitized by replacing NaNs and infinities with finite values to ensure numerical stability.

For class-conditional schedules, schedule updates are applied only to classes present in the current batch; in distributed settings, we synchronize the set of active classes across workers before applying optimizer steps to maintain consistent parameter updates.

Learning-rate schedule. We employ a linear warm-up for the first K_{ramp} king. After warm-up, the learning rate follows a mild decay schedule, with a decay factor applied after the midpoint of training. The learning rate of schedule parameters scales proportionally to the network learning rate.

EMA update. We maintain an exponential moving average of network parameters throughout training. The EMA half-life is specified in king units. Optionally, we apply an EMA ramp-up, where the effective half-life is bounded by the number of images seen so far during early training. EMA parameters are synchronized across workers in distributed settings.

Distributed training. For large-scale experiments (e.g., ImageNet-64), we use PyTorch Distributed Data Parallel (DDP) with NCCL backend. The global batch is evenly partitioned across workers. All parameters are broadcast from rank 0 at initialization. Gradients of network parameters are synchronized via DDP. Schedule parameters are explicitly all-reduced across workers, including zero-filled gradients for classes absent on a given worker, to guarantee consistent updates across GPUs.

Training budget and checkpoints. Across all datasets, fine-tuning processes approximately 1.2M images in total. We periodically save raw network weights, EMA weights, and schedule parameters. Unless otherwise specified, evaluation is performed using the final EMA checkpoint.

E Additional Experimental Analysis

Figures 2–5 visualize the learned schedules across datasets, subspace parameterizations, and conditioning schemes.

First, across all datasets (Figures 2–4), the learned anisotropic ratios deviate systematically from one over a substantial portion of the diffusion horizon, confirming that the two subspaces are not treated symmetrically by the learned schedule. However, the magnitude and shape of this deviation depend strongly on the dataset. For CIFAR-10 (Figure 2(b)) and AFHQv2 (Figure 3), the anisotropy ratio exhibits a smooth mid-horizon amplification before returning to one near the endpoints, suggesting that anisotropy is primarily active during intermediate diffusion times. In contrast, for FFHQ (Figure 4) the ratio shows a more pronounced early amplification followed by a gradual decay, indicating stronger low-frequency emphasis at early noise levels.

Second, on the class-conditional datasets (CIFAR-10 and ImageNet-64; Figures 2 and 5), class-conditional training induces clear inter-class variability in both isotropic and anisotropic schedules. In CIFAR-10 (Figure 2(c,d)), the class-conditional isotropic schedules display substantial dispersion around the geometric mean, and the anisotropic schedules further amplify these differences. On ImageNet-64 (Figure 5(a–f)), this effect becomes more structured: while class-conditional isotropic schedules vary moderately, the anisotropic variants reveal consistent class-dependent shifts in both geometric means and anisotropy ratios. Notably, the PCA-based conditional schedules in Figure 5(d–f) exhibit tighter concentration than their DCT counterparts (Figure 5(b,c)), suggesting that class-adaptive subspaces reduce unnecessary variability.

F Geometric Structure of Learned Subspaces

F.1 PCA Visualization

To analyze the geometry of the learned PCA subspaces, we first visualize the leading principal components for representative classes (cat, dog, airplane) in Figure 6. Each row shows the top principal directions reshaped into spatial patterns. We observe that semantically related classes (e.g., cat and dog) exhibit qualitatively similar dominant spatial structures, whereas structurally distinct classes (e.g., airplane) show noticeably different patterns.

To quantify cross-class similarity, we compute pairwise distances between subspaces using the Frobenius norm of projector differences, i.e.,

$$d(Q_1, Q_2) = \frac{\|Q_1 Q_1^\top - Q_2 Q_2^\top\|_F}{\sqrt{2k}},$$

where Q_1, Q_2 are orthonormal bases. We then apply classical multidimensional scaling (MDS) to embed this distance matrix into two dimensions for visualization. MDS constructs a low-dimensional embedding whose pairwise Euclidean distances best approximate the original subspace distances. Figure 7 reveals clear semantic clustering, with animal classes grouped together and separated from vehicle classes.

These observations suggest that the learned PCA subspaces capture semantically meaningful geometric structure.

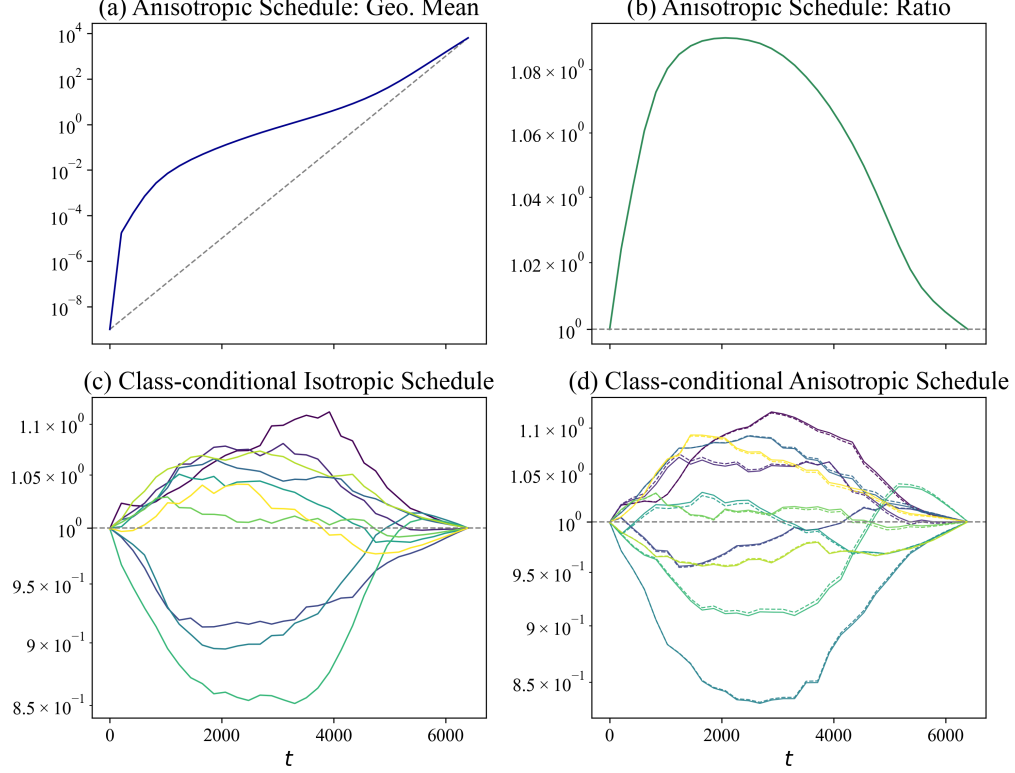


Figure 2: **CIFAR-10 learned schedule analysis.** (a) PCA-based geometric mean $\sqrt{g_1^{\text{PCA}}(t)g_2^{\text{PCA}}(t)}$ with a log-linear reference (gray dashed; log y -axis). (b) PCA anisotropy ratio $g_1^{\text{PCA}}(t)/g_2^{\text{PCA}}(t)$. (c) Class-conditional isotropic schedules $g_y(t)/\bar{g}(t)$, where $\bar{g}(t) = (\prod_{y=1}^C g_y(t))^{1/C}$ with $C = \text{\#class} = 10$. (d) Class-conditional anisotropic schedules over DCT subspaces: $g_{k,y}^{\text{DCT}}(t)/\bar{g}_k(t)$ for $k \in \{1, 2\}$ (solid/dashed), where i indexes classes and $\bar{g}_k(t)$ is the geometric mean across classes.

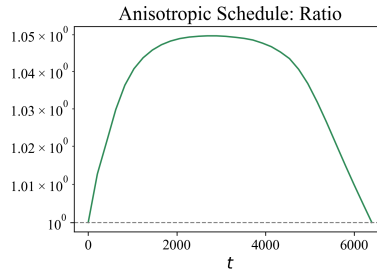


Figure 3: **AFHQv2 learned schedule analysis.** Ratio between the two learned DCT-based schedules $g_1^{\text{DCT}}(t)$ and $g_2^{\text{DCT}}(t)$ over time.

F.2 2D-DCT Transform Visualization

Let H be the image side length and $d = H^2$. The two-dimensional DCT (type-II) basis over $\mathbb{R}^{H \times H}$ is defined as follows. For each pair $(p, q) \in \{0, \dots, H-1\}^2$, the basis is

$$\Phi_{p,q}(x, y) = \gamma_p \gamma_q \cos\left(\frac{(2x+1)p\pi}{2H}\right) \cos\left(\frac{(2y+1)q\pi}{2H}\right),$$

$$x, y = 0, \dots, H-1.$$

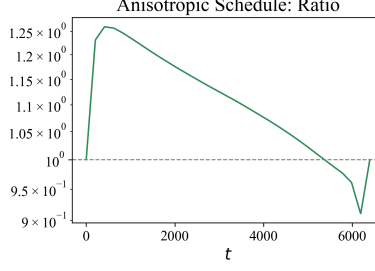


Figure 4: **FFHQ learned schedule analysis.** Ratio between the two learned DCT-based schedules $g_1^{\text{DCT}}(t)$ and $g_2^{\text{DCT}}(t)$ over time.

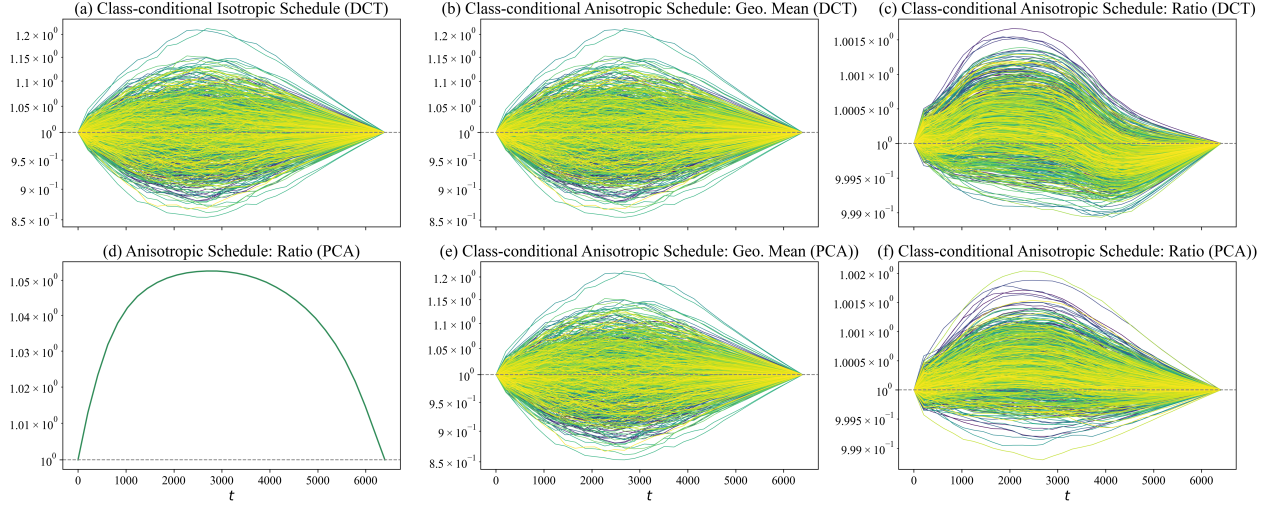


Figure 5: **ImageNet-64 learned schedule analysis.** (a) Class-conditional isotropic schedules shown as $g_y(t)/\bar{g}(t)$, where $\bar{g}(t)$ denotes the geometric mean across classes. (b) Class-conditional anisotropic schedules summarized by the geometric mean $\sqrt{g_{1,y}^{\text{DCT}}(t)g_{2,y}^{\text{DCT}}(t)}$ and normalized by its class-wise geometric mean. (c) Class-conditional anisotropy ratios $g_{1,y}^{\text{DCT}}/g_{2,y}^{\text{DCT}}$. (d) PCA-based (class-conditional basis) anisotropic schedule ratio $g_{1,y}^{\text{PCA}}(t)/g_{2,y}^{\text{PCA}}(t)$. (e) PCA-based (class-conditional basis) class-conditional anisotropic schedules shown as $\sqrt{g_{1,y}^{\text{PCA}}(t)g_{2,y}^{\text{PCA}}(t)}$ normalized by the geometric mean across classes. (f) PCA-based (class-conditional basis) class-conditional anisotropy ratios $g_{1,y}^{\text{PCA}}(t)/g_{2,y}^{\text{PCA}}(t)$. All ratios are plotted on a logarithmic y -axis, and dashed horizontal lines indicate the reference value 1.

with normalization factors

$$\gamma_p = \begin{cases} H^{-1/2}, & p = 0, \\ \sqrt{2}H^{-1/2}, & p > 0, \end{cases} \quad \gamma_q = \begin{cases} H^{-1/2}, & q = 0, \\ \sqrt{2}H^{-1/2}, & q > 0. \end{cases}$$

Vectorizing each $\Phi_{p,q}$ into \mathbb{R}^d and enumerating them yields the orthonormal basis $\{v_1, \dots, v_{H^2}\}$, which are the 2D-DCT basis of \mathbb{R}^d . Please refer to Figure 8 for example 2D-DCT bases.

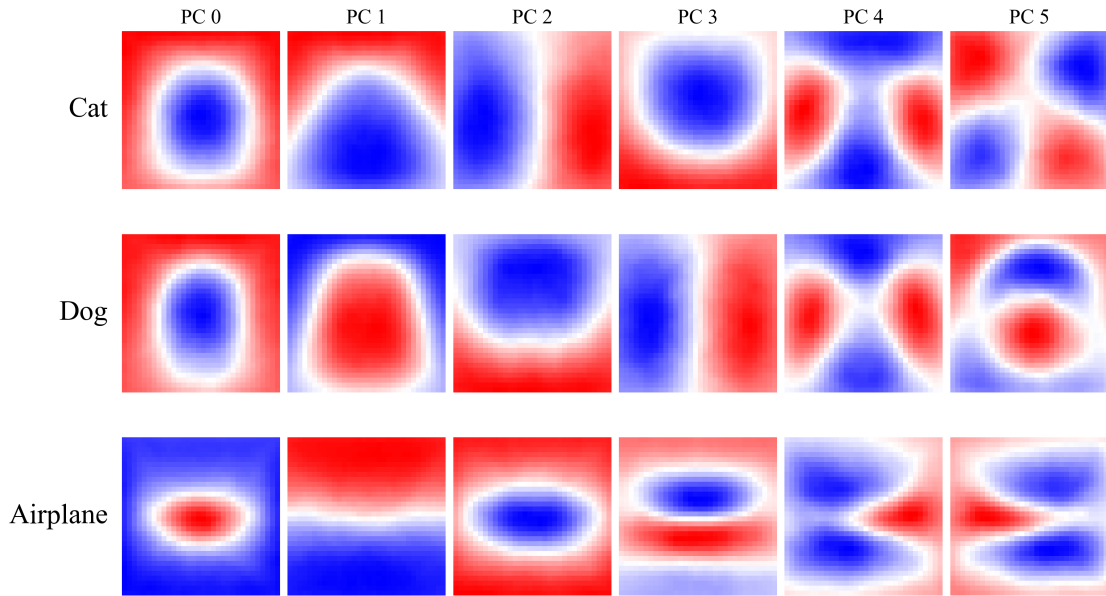


Figure 6: **Class-specific PCA subspaces.** Leading principal components for representative CIFAR-10 classes (cat, dog, airplane), reshaped as spatial patterns. Semantically related classes (e.g., cat and dog) exhibit qualitatively similar dominant structures, whereas visually distinct classes (e.g., airplane) display different principal directions.

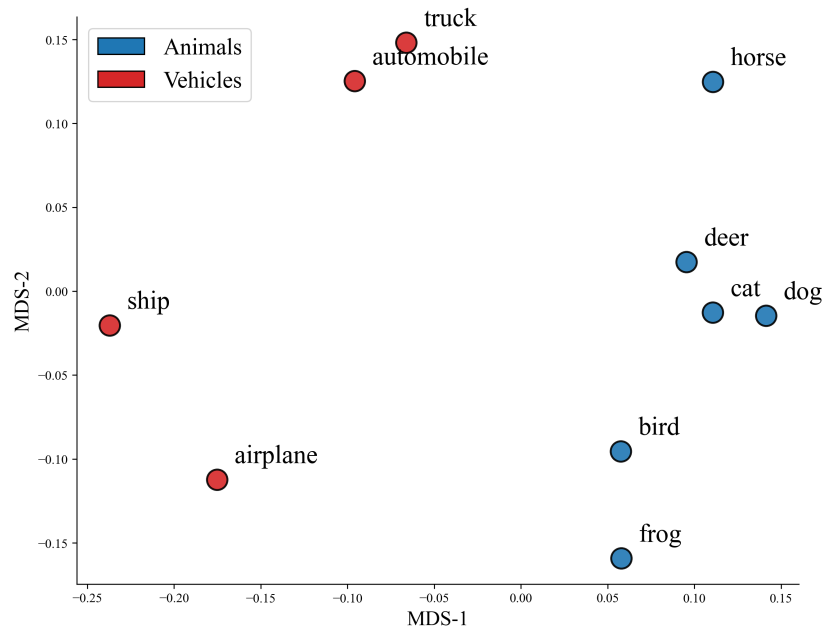


Figure 7: **Subspace distance embedding via classical MDS.** Pairwise distances between class-specific PCA subspaces are computed using the Frobenius norm between orthogonal projectors. Classical multidimensional scaling (MDS) embeds the resulting distance matrix into two dimensions. Animal classes cluster together and are separated from vehicle classes, indicating that the learned subspaces capture semantically structured geometry.

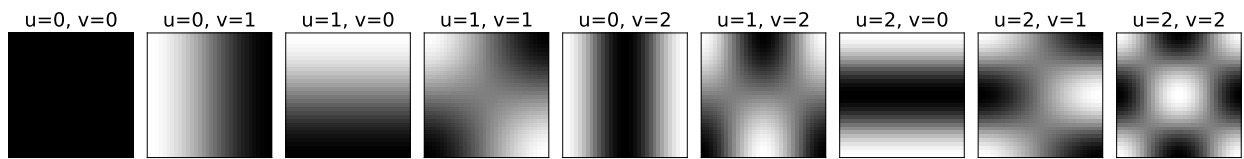


Figure 8: The first nine 2D-DCT bases ordered by increasing frequency.